



HAL
open science

Frictional Contact Solving for Material Point Method

Etienne Ménager, Justin Carpentier

► **To cite this version:**

Etienne Ménager, Justin Carpentier. Frictional Contact Solving for Material Point Method. 2026. <hal-05488708>

HAL Id: hal-05488708

<https://hal.science/hal-05488708v1>

Submitted on 2 Feb 2026

HAL is a multi-disciplinary open access archive for the deposit and dissemination of scientific research documents, whether they are published or not. The documents may come from teaching and research institutions in France or abroad, or from public or private research centers.

L'archive ouverte pluridisciplinaire HAL, est destinée au dépôt et à la diffusion de documents scientifiques de niveau recherche, publiés ou non, émanant des établissements d'enseignement et de recherche français ou étrangers, des laboratoires publics ou privés.



HAL Authorization

Frictional Contact Solving for Material Point Method

Etienne Ménager* and Justin Carpentier*

Abstract—Accurately handling contact with friction remains a core bottleneck for Material Point Method (MPM), from reliable contact point detection to enforcing frictional contact laws (non-penetration, Coulomb friction, and maximum dissipation principle). In this paper, we introduce a frictional-contact pipeline for implicit MPM that is both precise and robust. During the collision detection phase, contact points are localized with particle-centric geometric primitives; during the contact resolution phase, we cast frictional contact as a Nonlinear Complementarity Problem (NCP) over contact impulses and solve it with an Alternating Direction Method of Multipliers (ADMM) scheme. Crucially, the formulation reuses the same implicit MPM linearization, yielding efficiency and numerical stability. The method integrates seamlessly into the implicit MPM loop and is agnostic to modeling choices, including material laws, interpolation functions, and transfer schemes. We evaluate it across seven representative scenes that span elastic and elasto-plastic responses, simple and complex deformable geometries, and a wide range of contact conditions. Overall, the proposed method enables accurate contact localization, reliable frictional handling, and broad generality, making it a practical solution for MPM-based simulations in robotics and related domains.

I. INTRODUCTION

Accurately handling contact in deformable simulation is essential for robotics systems, where robots make and break contact to move or manipulate objects [1], [2], [3], [4]. While the Finite Element Method (FEM) supports soft-body simulation [5], [6], large deformations, remeshing, and path-dependent plasticity remain challenging. The Material Point Method (MPM) offers a compelling alternative. MPM mixes an Eulerian and a Lagrangian view of matter: the Lagrangian view represents each body as a set of material points (particles). In contrast, the Eulerian view advances dynamics on a background computational grid. The particle’s state is projected to the grid, where the equations of motion are solved; the updated grid state is then mapped back to particles. This dual view enables large deformation and complex constitutive behavior without remeshing [7], [8] and has been leveraged in recent robotics works for differentiable control and learning [9], [10], [11].

Yet, robust frictional contact remains a bottleneck for MPM. Detection is often performed on grid nodes. When two materials contribute mass to the same grid node, a contact is inferred and a normal is built from mass/volume gradients [12], [13], [14], [15]. This approach is robust, but intrinsically diffuse at the cell scale. Boundary-aware

alternatives improve geometry - e.g., particle-boundary level-set [16], [17], cell/sub-cell integration near interfaces [17], boundary material points [18], [19], hybrid MPM / discrete elements scheme [20], [21], [22] - but typically add modeling layers or penalties, and are frequently coupled to explicit stepping. On the resolution side, classical node-based approaches enforce no-penetration and no-slip implicitly by sharing the same interpolation space at a standard grid node [12]. Many methods remain local and sequential: a normal reaction from velocity projection or penalty is computed nodewise, then tangential forces are calculated using Coulomb law [17], [18], [23], [15]. These methods require penalty tuning and ignore global coupling between contacts. Recent convex formulations [24], [25] restore global structure but approximate the original complementarity model and introduce regularization choice.

To overcome these limits, we target both collision detection and collision resolution. For collision detection, we localize contacts at a sub-cell scale from particle-centric, geometry-aware primitives. For collision resolution, we cast frictional contact as a Nonlinear Complementarity Problem (NCP) on contact impulses and solve it with an Alternating Direction Method of Multipliers (ADMM)-based scheme, following rigid-body and FEM formulations in robotics [26], [27]. We implement the pipeline inside an implicit MPM loop to enable large time steps and to reuse the same linearization already factored for internal mechanics and constraints. The method integrates naturally in MPM, remains agnostic to material laws, interpolation and transfer schemes, and scales to multi-object scenes. We evaluate seven representative scenarios spanning elastic and elasto-plastic behavior, sticking–sliding transitions, and diverse geometries, demonstrating precise contact localization, robust frictional resolution, and broad compatibility.

This paper is organized as follows. Section II introduces MPM notation and implicit stepping. Section III details detection and frictional-contact resolution within implicit MPM. Section IV presents experiments, and Section V concludes and outlines future directions.

II. BACKGROUND AND NOTATIONS

This section recalls the continuum equations we simulate and derives the implicit MPM we use throughout the paper. We emphasize the mixed Eulerian-Lagrangian view, highlighting (i) how particle and grid exchange information, (ii) how the implicit linearization produces the admittance matrix that is later reused for contact, and (iii) how constitutive laws

*Both authors are in Inria and Département d’Informatique de l’École Normale Supérieure, PSL Research University in Paris, 75013 Paris, France. email: etienne.menager@inria.fr, justin.carpentier@inria.fr

and plasticity fit into this pipeline. We close this section with the contact-space notation employed by our solver. We refer the reader to [8] for a detailed description of MPMs

A. Continuum model

Let Ω_0 be the reference configuration (undeformed body at $t = 0$), and let $\mathbf{X} \in \Omega_0$ be a material point. The current position of the material point is $\mathbf{x}(\mathbf{X}, t)$, with deformation gradient $\mathbf{F} = \frac{\partial \mathbf{x}}{\partial \mathbf{X}}$ and volume variation $J = \det \mathbf{F}$. Balance of linear momentum in the reference frame is written as:

$$\rho_0 \ddot{\mathbf{x}} = \nabla_{\mathbf{X}} \cdot \mathbf{P} + \rho_0 \mathbf{f}, \quad (1)$$

where ρ_0 is the reference density, \mathbf{f} the body force, and \mathbf{P} the first Piola-Kirchhoff stress. For hyperelastic material with energy W , $\mathbf{P} = \frac{\partial W}{\partial \mathbf{F}}$. Boundary conditions complete the model. In MPM, we discretize the weak form of (1). This leads to the particle-sums that appear in the formulas below.

B. MPM: mixing Lagrangian particles and an Eulerian grid

MPM combines two representations of the same body. The Lagrangian view stores material history on a finite set of particles p , carrying mass m_p , volume V_p , position \mathbf{x}_p , velocity \mathbf{v}_p , deformation gradient \mathbf{F}_p , and possible internal variables (e.g., relative to plasticity). The Eulerian view uses a background grid as a computational backend to solve the momentum equation. At each step, particles transfer mass and momentum to nearby grid nodes through interpolation. The grid then performs the time update, and the updated grid state is interpolated back to the particles.

Let $N_i(\mathbf{x})$ be the interpolation function of grid node i , $N_{ip} = N_i(\mathbf{x}_p)$ and $\nabla N_{ip} = \nabla N_i(\mathbf{x})|_{\mathbf{x}_p}$. Let n denote the current time-step index. The particle-to-grid (P2G) transfer accumulates nodal mass and momentum on the grid,

$$\begin{aligned} m_i &= \sum_p m_p N_{ip}, \\ \mathbf{p}_i &= \sum_p m_p \mathbf{v}_p N_{ip}, \end{aligned} \quad (2)$$

and computes internal nodal forces from particle stresses based on virtual-work,

$$\mathbf{f}_i^{\text{int}} = - \sum_p V_p \mathbf{P}_p \nabla N_{ip}. \quad (3)$$

External forces \mathbf{f}^{ext} (e.g., gravity) are either added on the grid or on the particles and transferred to the grid using an interpolation function.

After the grid update (see Section II-C), grid-to-particle (G2P) interpolates velocities and positions back,

$$\begin{aligned} \mathbf{v}_p^{n+1} &= \sum_i N_{ip} \mathbf{v}_i^{n+1}, \\ \mathbf{x}_p^{n+1} &= \mathbf{x}_p^n + \Delta t \mathbf{v}_p^{n+1}, \end{aligned} \quad (4)$$

and advances the deformation gradient with the grid velocity gradient,

$$\mathbf{F}_p^{n+1} = (\mathbf{I} + \Delta t \sum_i \mathbf{v}_i^{n+1} \otimes \nabla N_{ip}) \mathbf{F}_p^n. \quad (5)$$

Stresses are then recomputed at particles from \mathbf{F}_p^{n+1} .

C. Implicit time stepping and the admittance matrix

We adopt an implicit update on the grid for stability and larger time steps. Linearizing the discrete equations over a time step Δt yields a symmetric positive-definite system for the stacked nodal velocity increment $\Delta \mathbf{v} = \mathbf{v}^{n+1} - \mathbf{v}^n \in \mathbb{R}^{3n_g}$

$$\underbrace{(\mathbf{M} + \Delta t \mathbf{D} + \Delta t^2 \mathbf{K})}_{\mathbf{A}} \Delta \mathbf{v} = \underbrace{\Delta t (\mathbf{f}^{\text{ext}} - \mathbf{f}^{\text{int}})}_{\mathbf{b}} + \text{Lagrange multipliers}, \quad (6)$$

where n_g is the number of grid nodes, $\mathbf{M} = \text{diag}(m_i)$ is the lumped mass, \mathbf{D} is the damping matrix (computed here as Rayleigh damping), and \mathbf{K} the tangent stiffness arising from the variation of internal forces. \mathbf{A}^{-1} is the admittance matrix we will reuse for contact solving. Solving $\mathbf{A} \Delta \mathbf{v} = \mathbf{b}$ gives $\mathbf{v}^{n+1} = \mathbf{v} + \Delta \mathbf{v}$.

The stiffness matrix \mathbf{K} is computed from (3). A perturbation of nodal velocities perturbs \mathbf{F}_p via the grid velocity gradient, which in turn perturbs \mathbf{P}_p . Collecting contributions over particles yields \mathbf{K} as a sparse block matrix whose entries depend on $\frac{\partial \mathbf{P}_p}{\partial \mathbf{F}_p}$, \mathbf{F}_p , and ∇N_{ip} .

D. Transfer and interpolation for stability

Basic transfers can be affected by dissipation and cell-crossing artifacts. Several approaches exist to improve stability. Affine Particle-In-Cell (APIC) [28] augments particles with an affine velocity that preserves angular momentum and reduces numerical diffusion. Moving Least Squares MPM (MLS-MPM) reconstructs grid and particle velocities using moving least squares to handle strong distortion better. Regarding interpolation, higher-order B-spline interpolation [29] enlarges the support and yields smoother gradients. More recently, CK-MPM [30] proposes a \mathcal{C}^2 compact kernel and a dual-grid framework that mitigates cell-crossing with reduced numerical diffusion, while remaining compatible with APIC/MLS, offering a stable and efficient alternative to wide B-spline supports.

E. Constitutive behavior and plasticity

We support standard elastic and hyperelastic laws (linear, St. Venant-Kirchhoff, co-rotational, and Neo-Hookean) as well as elasto-plastic extensions. Plasticity is handled at particles by the multiplicative split $\mathbf{F} = \mathbf{F}_e \mathbf{F}_{pla}$: after the elastic trial update, a plastic projection (e.g., SVD-based projection) enforces the yield constraints and updates \mathbf{F}_{pla} . Stresses $\mathbf{P}(\mathbf{F}_e)$ then follow from the post-projection state. This particle-level mechanism allows considering plasticity while keeping the grid unchanged.

F. Contact notation

To couple contact consistently with the implicit step, we map grid velocities to relative velocities at contact points via a contact Jacobian \mathbf{H}_c . For a set of contact frames c with normal \mathbf{n}_c and tangents $\mathbf{t}_{c,1}, \mathbf{t}_{c,2}$, the stacked contact velocity is $\boldsymbol{\sigma}_c = \mathbf{H}_c \mathbf{v}$, and the contact force is $\boldsymbol{\lambda}_c = [\lambda_{c,N}, \boldsymbol{\lambda}_{c,T}]$ constrained by a Coulomb cone. The Delassus operator $\mathbf{G} = \mathbf{H}_c \mathbf{A}^{-1} \mathbf{H}_c^\top$ encodes how forces change contact velocities. Advancing the grid without contact yields a free contact

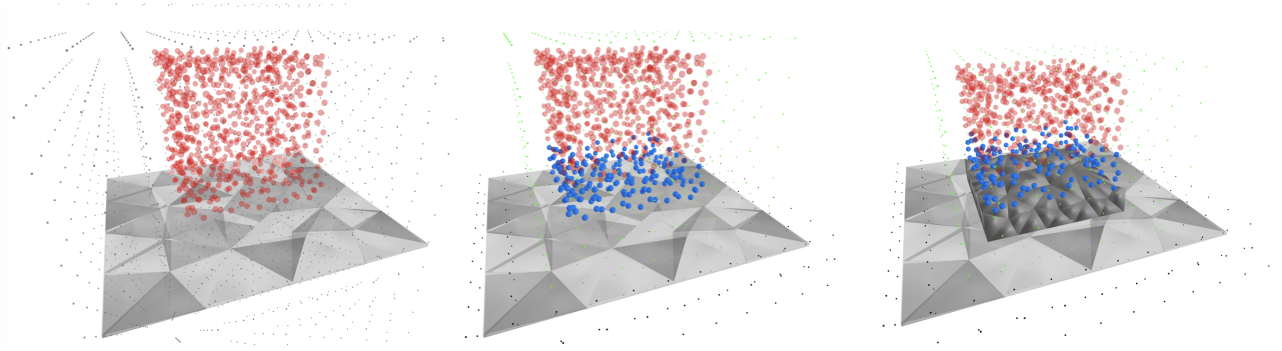


Fig. 1: Particle-centric contact detection and grid-based resolution. **Left:** A block is discretized into particles (red) and falls onto a planar surface meshed with tetrahedra (gray). Gray dots represent MPM grid nodes. **Center:** (broad phase) Overlaps between particle supports (green) and tetrahedral supports (black) on a shared grid yield candidate pairs. Particles selected for the narrow phase are shown in blue. **Right:** (narrow phase and solve) For each candidate (blue), the associated deformed tetrahedron (dark gray) is used to localize contact points and frames. Contacts are deposited onto the tetrahedra vertices and then transferred to grid nodes to assemble the contact Jacobian. The global frictional contact is written as an NCP and solved by ADMM. Grid velocities are corrected by the resulting contact impulses and mapped back to particles.

velocity $\mathbf{g} = \mathbf{H}_c \mathbf{v}^{\text{free}}$, contact then corrects it by solving a friction problem in $\boldsymbol{\lambda}_c$. The following section formalizes this as a nonlinear complementarity problem.

III. FRICTIONAL CONTACT FOR IMPLICIT MPM

This section details how we discretize contact between particles with geometry-aware detection, deposit contact frames into the grid, and enforce frictional contact as a global NCP on the grid, solved using ADMM. We end with remarks on compatibility and multi-object scenes. Figure 1 illustrates the particle-centric detection and grid-based resolution.

A. Contact discretization on particles

Broadphase. We select potentially interacting pairs using a uniform background grid shared across objects. Overlapping cells yield candidate particle pairs (or particle-tetrahedron pairs for mesh obstacles). This reduces complexity and is independent of the MPM grid used for dynamics.

Narrowphase. Contacts are then localized from deformed particle primitives. Each particle carries a tetrahedron whose vertices are advected by the particle’s deformation gradient. We query tetrahedron-tetrahedron proximity using a variation of the GJK algorithm [31]. For each detected contact, we compute:

- a contact point \mathbf{x}_c on the deformed primitives;
- a unit normal \mathbf{n}_c ;
- an orthonormal contact frame $\mathbf{R}_c = [\mathbf{t}_{c,1}, \mathbf{t}_{c,2}, \mathbf{n}_c]$.

This particle-centric, geometry-aware detection provides sub-cell localization, in contrast to node-wise grid detection, and ensures the contact geometry is consistent with the actual deformable shape.

B. Grid deposition of contact frames

Contacts are enforced on the grid, so each contact must couple to nearby grid nodes. We process in two steps.

Step 1 - Barycentric lift to tetrahedron vertices. A contact point \mathbf{x}_c lying inside a deformed tetrahedron with vertices $\{\mathbf{x}_k\}_{k=1..4}$ is expressed with barycentric weights $\{\phi_k\}$ such that $\mathbf{x}_c = \sum_k \phi_k \mathbf{x}_k$. To ensure active nodal support, we replace the contacting particle by four vertex proxies at $\{\mathbf{x}_k\}$. Proxy k carries barycentric weight ϕ_k . P2G deposits contact through these proxies, rather than the particle centroid, thereby avoiding empty-cell contacts and ensuring deposition only on nodes with mass.

Step 2 - Vertex-to-grid interpolation. Each vertex contributes to grid nodes i through the same interpolation $N_i(\cdot)$ as in the P2G/G2P pipeline. Stacking nodal velocities into $\mathbf{v} \in \mathbb{R}^{3n_g}$, the contact Jacobian row block $\mathbf{H}_{c,j} \in \mathbb{R}^{3 \times 3n_g}$ maps nodal velocities to contact-frame j relative velocity:

$$\boldsymbol{\sigma}_{c,j} = \begin{bmatrix} v_{t,1} \\ v_{t,2} \\ v_n \end{bmatrix} = \mathbf{H}_{c,j} \mathbf{v}, \quad (7)$$

with

$$\mathbf{H}_{c,j} = \sum_{k=1}^4 \phi_k \sum_{i \in \mathcal{N}(k)} \begin{bmatrix} \mathbf{t}_{c,1} \\ \mathbf{t}_{c,2} \\ \mathbf{n}_c \end{bmatrix}_j \otimes N_i(\mathbf{x}_k) \mathbf{e}_i^\top, \quad (8)$$

where $\mathcal{N}(k)$ are grid nodes influencing vertex k , and \mathbf{e}_i selects node i ’s 3-DOF block. The global Jacobian matrix is obtained by stacking all contact Jacobian rows. This barycentric deposition guarantees active nodal support and preserves geometric locality.

C. Global frictional contact as an NCP on the grid

Contact modeling involves various complementarity physical principles [32]. First, the so-called Signorini condition provides a complementarity constraint $0 \leq \lambda_{c,N} \perp \sigma_{c,N} \geq 0$, where N stands for the normal component of the contact force and contact point velocity. The Signorini condition ensures that the normal force is repulsive, the bodies do not interpenetrate, and the power injected by normal contact

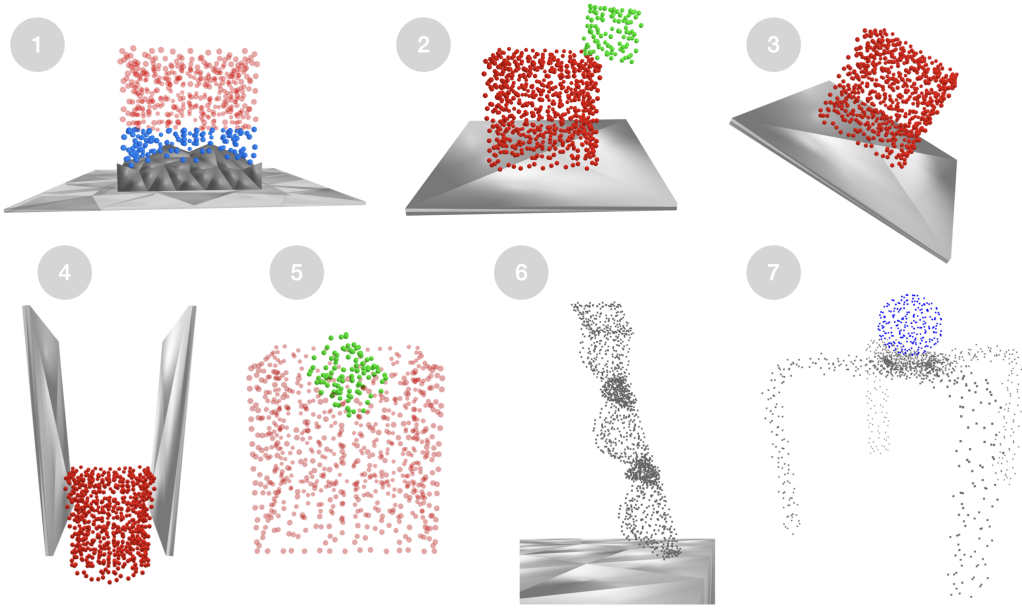


Fig. 2: Illustration of the seven experiments used in this paper: (1) a cube falling onto a plane; (2) multi-object interaction; (3) a cube sliding on an inclined plane; (4) a plastic cube sliding between two vertical planes; (5) a cube falling into a fluid-like medium; (6) a soft robotic finger rubbing against a plane; (7) a sphere impacting a quadrupod soft robot.

forces is null. Secondly, the maximum dissipation principle combined with the frictional Coulomb law $\|\boldsymbol{\lambda}_{c,T}\|_2 \leq \mu \boldsymbol{\lambda}_{c,N}$ of friction μ , states that the tangential component of the contact forces $\boldsymbol{\lambda}_{c,T}$ maximizes the power dissipated by the contact. These principles are equivalent to the following NCP:

$$\begin{aligned} \mathcal{K}_\mu \ni \boldsymbol{\lambda}_c \perp \boldsymbol{\sigma}_c + \Gamma_\mu(\boldsymbol{\sigma}_c) \in \mathcal{K}_\mu^* \\ \boldsymbol{\sigma}_c = \mathbf{G}\boldsymbol{\lambda}_c + \mathbf{g} \end{aligned} \quad (9)$$

where \mathbf{G} is the so-called Delassus matrix that gives the admittance matrix \mathbf{A}^{-1} projected on the contacts and enables to map contact forces to contact points velocities, \mathbf{g} is the free velocity of the contact points when $\boldsymbol{\lambda}_c = \mathbf{0}$, \mathcal{K}_μ is a second-order cone with aperture angle $\text{atan}(\mu)$, \mathcal{K}_μ^* is the dual cone of \mathcal{K}_μ , and $\Gamma_\mu(\boldsymbol{\sigma}_c) = [0, 0, \mu \|\boldsymbol{\sigma}_{c,T}\|_2]$ is the De Saxcé correction enforcing the Signorini condition [33], [32]. This NCP can be solved to find the value of $\boldsymbol{\lambda}_c$ using different optimization methods, like Projected Gauss-Seidel methods (PGS) [34], [32] or ADMM [34], [26].

In the case of the MPM, the implicit MPM step produces the admittance matrix \mathbf{A}^{-1} and the free grid velocity (no contact) $\mathbf{v}^{\text{free}} = \mathbf{v}^n + \mathbf{A}^{-1}\mathbf{b}$. In contact space, the free relative velocity is $\mathbf{g} = \mathbf{H}_c \mathbf{v}^{\text{free}}$. The solution of the NCP is the contact impulses $\boldsymbol{\lambda}_c$ that correct grid velocities by

$$\begin{aligned} \mathbf{v}^{n+1} &= \mathbf{v}^{\text{free}} + \mathbf{A}^{-1} \mathbf{H}_c^\top \boldsymbol{\lambda}_c, \\ \boldsymbol{\sigma}_c &= \mathbf{H}_c \mathbf{v}^{n+1} = \mathbf{g} + \mathbf{G}\boldsymbol{\lambda}_c, \end{aligned} \quad (10)$$

where the Delassus operator $\mathbf{G} = \mathbf{H}_c \mathbf{A}^{-1} \mathbf{H}_c^\top$ couples contacts globally.

We solve (9) with an ADMM scheme (as used in rigid-body and FEM simulation [26], [27]), alternating a linear

step and a proximal projection onto the friction cone. The stopping criteria are based on the tracking of the primal/dual residuals associated with the NCP. We refer to [26] for more details.

Algorithm 1: MPM simulation with frictional contacts.

Initialize: a set of particles $\{p\}$ per object, a background grid per object;
for $k = 0, 1, \dots, K$ **do**
 Step 1: P2G and assembly of \mathbf{A} , \mathbf{b} ; factorize \mathbf{A} (once per object);
 Step 2: Free step: $\mathbf{v}^{\text{free}} = \mathbf{v}^n + \mathbf{A}^{-1}\mathbf{b}$;
 Step 3: Detection on particles and creation of the contact frames $[\mathbf{x}_c, \mathbf{R}_c]$;
 Step 4: Build \mathbf{H}_c by baricentric lift to tetrahedron vertices, then vertex-to-grid deposition ;
 Step 5: ADMM solve of (9) using $\mathbf{G} = \mathbf{H}_c \mathbf{A}^{-1} \mathbf{H}_c^\top$ and $\mathbf{g} = \mathbf{H}_c \mathbf{v}^{\text{free}}$;
 Step 6: Correct grid velocity $\mathbf{v}^{n+1} = \mathbf{v}^{\text{free}} + \mathbf{A}^{-1} \mathbf{H}_c^\top \boldsymbol{\lambda}_c$;
 Step 7: G2P update of particles;
end

D. Compatibility and multi-object simulation

The global approach is summarized in Algorithm 1. It is agnostic to constitutive models and transfer/interpolation; it only requires consistent P2G/G2P and the admittance matrix \mathbf{A}^{-1} . For multi-object simulation, we maintain one MPM grid per object, with a shared origin and spacing. The contact Jacobian concatenates per-object blocks, and the

TABLE I: Cube-on-ground results. Experiments are organized by interpolation (L: Linear, Q: Quadratic, C: CK), transfer (B: Basic, A: APIC, M: MLS), and material (L: Linear, S: St. Venant–Kirchhoff, C: Co-rotational, N: Neo-Hookean). **Abbreviations** — #C: mean number of active contact points; Iter.: mean ADMM iterations per step; Mean res.: mean final ADMM residual; Max res.: maximum final ADMM residual; % steps $\leq 10^{-6}$: fraction of time steps whose final residual is $\leq 10^{-6}$.

Exp.	#C (mean)	Iter. (mean)	Mean res.	Max res.	% steps $\leq 10^{-6}$
LBN	59.7	613.14	3.11×10^{-6}	3.49×10^{-5}	71.85%
QBN	95.4	518.02	1.76×10^{-6}	7.80×10^{-6}	77.32%
LAN	56.8	580.49	2.34×10^{-6}	2.80×10^{-5}	79.85%
QAN	88.1	481.33	2.15×10^{-6}	1.33×10^{-5}	75.50%
CAN	46.1	274.26	6.49×10^{-6}	6.25×10^{-4}	84.03%
CMN	54.3	300.90	1.41×10^{-6}	1.37×10^{-5}	80.87%
CML	58.3	313.61	1.53×10^{-6}	1.37×10^{-5}	80.73%
CMS	61.0	333.22	8.91×10^{-6}	7.90×10^{-4}	76.63%
CMC	68.2	293.97	1.48×10^{-6}	1.24×10^{-5}	85.11%

ADMM absolute tolerance 10^{-6} ; maximum 1000 iterations per step.

Delassus contains cross-terms that couple objects through shared contact.

IV. EXPERIMENTS

All experiments are illustrated in Figure 2. Unless stated otherwise, we use quadratic B-spline interpolation; basic P2G/G2P, and a Neo-Hookean material. We also report results with linear, St. Venant-Kirchhoff, co-rotational elasticity, and APIC/CK-APIC/CK-MLS transfers. Particles are built from object meshes. We initialize one particle per mesh tetrahedron at its barycenter and attach that tetrahedral primitive to the particle. Time steps are $\Delta t \in [10^{-3}, 10^{-2}]$ s and grid spacing is chosen so that each active cell initially contains roughly 6-10 particles. Collision detection uses Coal [35] on deformed particle tetrahedra during the narrowphase. The frictional contact is solved by the ADMM-based approach proposed in [26], with a sparse linear backend leveraging the implicit MPM factorization. We set an absolute tolerance of 10^{-6} and cap at 1000 iterations per simulation step.

Experiment 1 - Drop on a fixed plane. A deformable block falls onto a fixed floor. Across materials and transfers, the ADMM residual is sub-millimetric - typical accuracy for soft robotics - and reaches 10^{-6} in more than 75% of the time steps. The average number of active contacts varies with the constitutive law and the transfer scheme. This experiment validates end-to-end integration of detection, deposition, and global NCP resolution. The results are shown in Table I.

Experiment 2 - Multi-object simulation. A block falls onto another block resting on a fixed floor, with several initial offsets. The Delassus operator \mathbf{G} couples contacts across bodies, handling simultaneous normal/tangential constraints and contact mode switches without penalty tuning.

Experiment 3 - Sliding on an inclined plane. The plane is rotated by -30° around the x -axis. We measure the block’s center of mass tangential speed along the plane while it remains in contact. As μ increases, the system exhibits the

expected stick-slip transition and approaches a critical μ beyond which the block no longer translates. Speeds are slightly negative near the threshold due to elastic compliance (small recoil). Results are shown in Figure 3.

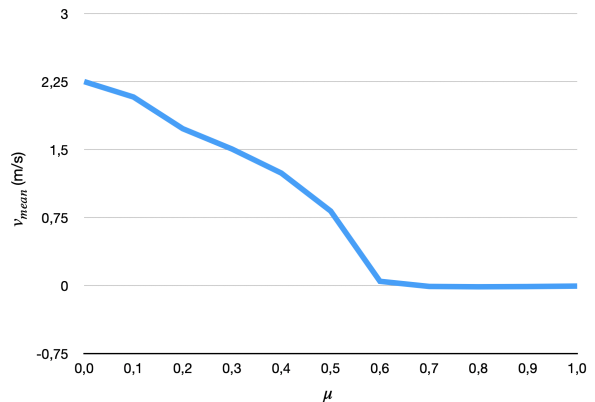


Fig. 3: Mean center-of-mass speed of the sliding cube along the plane direction as a function of the friction coefficient.

Experiment 4 - Plastic block between fixed walls. A plastic cube falls between two vertical planes. Contact dissipation and plastic flow interact: the block stops at a height that depends on friction and wall orientation, and the final shape reflects both wall friction and volumetric compaction.

Experiment 5 - Block entering a fluid-like medium. The red medium stores only volumetric pressure and uses deviatoric-eraser plasticity. Boundary conditions enforce zero velocity. The falling block penetrates while being slowed by frictional contact. Because the medium carries no shear memory, it does not close behind the intruder.

Experiment 6 - Soft finger rubbing a plane. A soft finger with base actuation translates laterally on a fixed plane. We observe sticking-breaking-sliding contact at the fingertip, consistent with Coulomb friction.

Experiment 7 - Sphere on a quadrupod soft robot. A sphere impacts a quadrupod soft robot, producing spatially distributed contacts over a complex geometry. Deformation patterns are governed by the frictional contacts.

V. CONCLUSION

In this paper, we introduced a frictional-contact pipeline that integrates naturally with implicit MPM Contacts are detected at the sub-cell scale using particle-centric geometry, deposited onto the grid with the exact interpolation employed by MPM, and resolved as a nonlinear complementarity problem involving contact impulses. Across elastic and elasto-plastic scenes, sliding, stick-slip transitions, multi-contact, and complex geometries, the approach provides precise contact localization, robust Coulomb friction, and broad compatibility with constitutive laws, transfer schemes, and interpolation choices.

As in any MPM pipeline, discretization has a significant impact on performance and accuracy. Our current implementation uses one grid per object with a shared origin and spatial resolution. Multi-resolution grids and multi-time stepping are not yet supported. For simulation with very large contact sets, forming and applying the Delassus operator (and related products) dominate the runtime. Although amortized by the implicit factorization, this remains the main computational bottleneck.

Promising directions include contact sparsification, warm-starting, and improved preconditioning for the ADMM solver, as well as multi-resolution grids and tight integration with differentiable simulation. These research directions could, for instance, exploit the differentiability of both implicit MPM and the ADMM contact layers for mechanical parameter identification, optimal design, and optimal control.

ACKNOWLEDGMENTS

This work has received support from the French government, managed by the National Research Agency, through the INEXACT project (ANR-22-CE33-0007-01) and under the France 2030 program with the references Organic Robotics Program (PEPR O2R) and “PR[AI]RIE-PSAI” (ANR-23-IACL-0008). The European Union also supported this work through the ARTIFACT project (GA no.101165695) and the AGIMUS project (GA no.101070165). Views and opinions expressed are those of the author(s) only and do not necessarily reflect those of the funding agencies.

REFERENCES

- [1] M. Teschner, S. Kimmerle, B. Heidelberger, G. Zachmann, L. Raghupathi, A. Fuhrmann, M.-P. Cani, F. Faure, N. Magnenat-Thalmann, W. Strasser, and P. Volino, “Collision detection for deformable objects,” *Comput. Graph. Forum*, vol. 24, no. 1, pp. 61–81, Mar. 2005.
- [2] E. Coevoet, A. Escande, and C. Duriez, “Optimization-based inverse model of soft robots with contact handling,” *IEEE Robotics and Automation Letters*, vol. 2, no. 3, pp. 1413–1419, 2017.
- [3] C. Della Santina, R. K. Katzschmann, A. Biechi, and D. Rus, “Dynamic control of soft robots interacting with the environment,” in *2018 IEEE International Conference on Soft Robotics (RoboSoft)*, 2018, pp. 46–53.
- [4] E. Ménager and C. Duriez, “Learning control strategy in soft robotics through a set of configuration spaces,” in *2024 IEEE 7th International Conference on Soft Robotics (RoboSoft)*. IEEE, 2024, pp. 263–269.
- [5] B. Caasenbrood, A. Pogromsky, and H. Nijmeijer, “Sorotoki: A matlab toolkit for design, modeling, and control of soft robots,” *IEEE Access*, vol. PP, pp. 1–1, 01 2024.
- [6] F. Faure, C. Duriez, H. Delingette, J. Allard, B. Gilles, S. Marchesseau, H. Talbot, H. Courtecuisse, G. Bousquet, I. Peterlik, *et al.*, “Sofa: A multi-model framework for interactive physical simulation,” *Soft tissue biomechanical modeling for computer assisted surgery*, pp. 283–321, 2012.
- [7] D. Sulsky, Z. Chen, and H. Schreyer, “A particle method for history-dependent materials,” *Computer Methods in Applied Mechanics and Engineering*, vol. 118, no. 1, pp. 179–196, 1994. [Online]. Available: <https://www.sciencedirect.com/science/article/pii/0045782594901120>
- [8] C. Jiang, C. A. Schroeder, J. Teran, A. Stomakhin, and A. Selle, “The material point method for simulating continuum materials,” *ACM SIGGRAPH 2016 Courses*, 2016. [Online]. Available: <https://api.semanticscholar.org/CorpusID:24134010>
- [9] Y. Hu, J. Liu, A. Spielberg, J. B. Tenenbaum, W. T. Freeman, J. Wu, D. Rus, and W. Matusik, “Chainqueen: A real-time differentiable physical simulator for soft robotics,” in *2019 International Conference on Robotics and Automation (ICRA)*. IEEE Press, 2019, p. 6265–6271. [Online]. Available: <https://doi.org/10.1109/ICRA.2019.8794333>
- [10] Z. Huang, Y. Hu, T. Du, S. Zhou, H. Su, J. B. Tenenbaum, and C. Gan, “Plasticinelab: A soft-body manipulation benchmark with differentiable physics,” in *International Conference on Learning Representations*, 2021. [Online]. Available: <https://openreview.net/forum?id=xCcDBRQEDW>
- [11] J. Gu, F. Xiang, X. Li, Z. Ling, X. Liu, T. Mu, Y. Tang, S. Tao, X. Wei, Y. Yao, X. Yuan, P. Xie, Z. Huang, R. Chen, and H. Su, “Maniskill2: A unified benchmark for generalizable manipulation skills,” in *International Conference on Learning Representations*, 2023. [Online]. Available: <https://openreview.net/pdf?id=b.CQDy9vrD1>
- [12] S. Bardenhagen, J. Guilkey, K. Roessig, J. Brackbill, W. Witzel, and J.C.Foster, “An improved contact algorithm for the material point method and application to stress propagation in granular material,” *Computer Modeling in Engineering & Sciences*, vol. 2, no. 4, pp. 509–522, 2001. [Online]. Available: <http://www.techscience.com/CMES/v2n4/24749>
- [13] P. Huang, X. Zhang, S. Ma, and X. Huang, “Contact algorithms for the material point method in impact and penetration simulation,” *Int. J. Numer. Methods Eng.*, vol. 85, no. 4, pp. 498–517, Jan. 2011.
- [14] W. Hu and Z. Chen, “A multi-mesh mpm for simulating the meshing process of spur gears,” *Computers & Structures*, vol. 81, no. 20, pp. 1991–2002, 2003. [Online]. Available: <https://www.sciencedirect.com/science/article/pii/S0045794903002608>
- [15] S. Nezamabadi, F. Radjai, J. Averseng, and J.-Y. Delenne, “Implicit frictional-contact model for soft particle systems,” *Journal of the Mechanics and Physics of Solids*, vol. 83, pp. 72–87, 2015. [Online]. Available: <https://www.sciencedirect.com/science/article/pii/S0022509615001568>
- [16] C. Liu and W. Sun, “Ils-mpm: An implicit level-set-based material point method for frictional particulate contact mechanics of deformable particles,” *Computer Methods in Applied Mechanics and Engineering*, vol. 369, p. 113168, 2020. [Online]. Available: <https://www.sciencedirect.com/science/article/pii/S0045782520303534>
- [17] J.-U. Song and H.-G. Kim, “A novel implicit cell-based material point method with particle boundaries and its application to contact problems,” *Computer Methods in Applied Mechanics and Engineering*, vol. 442, p. 118067, 2025. [Online]. Available: <https://www.sciencedirect.com/science/article/pii/S0045782525003391>
- [18] E. G. Kakouris, M. N. Chatzis, and S. P. Triantafyllou, “A high-fidelity material point method for frictional contact problems,” 2024. [Online]. Available: <https://arxiv.org/abs/2403.13534>
- [19] X. Han, T. F. Gast, Q. Guo, S. Wang, C. Jiang, and J. Teran, “A hybrid material point method for frictional contact with diverse materials,” *Proc. ACM Comput. Graph. Interact. Tech.*, vol. 2, no. 2, July 2019. [Online]. Available: <https://doi.org/10.1145/3340258>
- [20] H. Chen, S. Zhao, J. Zhao, and X. Zhou, “Dem-enriched contact approach for material point method,” *Computer Methods in Applied Mechanics and Engineering*, vol. 404, 11 2022.

- [21] C. Liu, Q. Sun, and G. G. D. Zhou, "Coupling of material point method and discrete element method for granular flows impacting simulations," *Int. J. Numer. Methods Eng.*, vol. 115, no. 2, pp. 172–188, July 2018.
- [22] Y. Yue, B. Smith, P. Y. Chen, M. Chantharayukhonthorn, K. Kamrin, and E. Grinspun, "Hybrid grains: adaptive coupling of discrete and continuum simulations of granular media," *ACM Trans. Graph.*, vol. 37, no. 6, Dec. 2018. [Online]. Available: <https://doi.org/10.1145/3272127.3275095>
- [23] M. A. Homel and E. B. Herbold, "Field-gradient partitioning for fracture and frictional contact in the material point method," *Int. J. Numer. Methods Eng.*, vol. 109, no. 7, pp. 1013–1044, Feb. 2017.
- [24] Z. Zong, C. Jiang, and X. Han, "A convex formulation of frictional contact for the material point method and rigid bodies," in *2024 IEEE/RSJ International Conference on Intelligent Robots and Systems (IROS)*. IEEE, 2024, pp. 1831–1838.
- [25] C. Yu, W. Du, Z. Zong, A. M. Castro, C. Jiang, and X. Han, "A convex formulation of material points and rigid bodies with gpu-accelerated async-coupling for interactive simulation," *CoRR*, 2025.
- [26] J. Carpentier, Q. Le Lidec, and L. Montaut, "From compliant to rigid contact simulation: a unified and efficient approach," in *RSS 2024- Robotics: Science and Systems (RSS)*, 2024.
- [27] E. Ménager, L. Montaut, Q. Le Lidec, and J. Carpentier, "Differentiable simulation of soft robots with frictional contacts," in *2025 IEEE 8th International Conference on Soft Robotics (RoboSoft)*. IEEE, 2025, pp. 1–8.
- [28] C. Jiang, C. Schroeder, A. Selle, J. Teran, and A. Stomakhin, "The affine particle-in-cell method," *ACM Transactions on Graphics (TOG)*, vol. 34, no. 4, pp. 1–10, 2015.
- [29] Y. Gan, Z. Sun, Z. Chen, X. Zhang, and Y. Liu, "Enhancement of the material point method using b-spline basis functions," *International Journal for Numerical Methods in Engineering*, vol. 113, 07 2017.
- [30] M. Liu, X. Wang, and M. Li, "Ck-mpm: A compact-kernel material point method," *ACM Transactions on Graphics (TOG)*, vol. 44, no. 4, pp. 1–14, 2025.
- [31] L. Montaut, Q. Le Lidec, V. Petrik, J. Sivic, and J. Carpentier, "Gjk++: Leveraging acceleration methods for faster collision detection," *IEEE Transactions on Robotics*, vol. 40, pp. 2564–2581, 2024.
- [32] Q. Le Lidec, W. Jallet, L. Montaut, I. Laptev, C. Schmid, and J. Carpentier, "Contact models in robotics: a comparative analysis," *IEEE Transactions on Robotics*, 2024.
- [33] G. DE SAXCE and Z.-Q. FENG, "The bipotential method: A constructive approach to design the complete contact law with friction and improved numerical algorithms," *Mathematical and computer modelling*, vol. 28, no. 4-8, pp. 225–245, 1998.
- [34] V. Acary, M. Brémond, and O. Huber, "On solving contact problems with coulomb friction: formulations and numerical comparisons," *Advanced Topics in Nonsmooth Dynamics: Transactions of the European Network for Nonsmooth Dynamics*, pp. 375–457, 2018.
- [35] J. Pan, S. Chitta, D. Manocha, F. Lamiraux, J. Mirabel, J. Carpentier, L. Montaut, *et al.*, "Coal: an extension of the flexible collision library," <https://github.com/coal-library/coal>, 2015–2024.